ACS Catalysis

pubs.acs.org/acscatalysis

Research Article

Active and Regioselective Ru Single-Site Heterogeneous Catalysts for Alpha-Olefin Hydroformylation

Francisco Javier Escobar-Bedia, Miguel Lopez-Haro, Jose Juan Calvino, Vlad Martin-Diaconescu, Laura Simonelli, Virginia Perez-Dieste, Maria J. Sabater, Patricia Concepción, and Avelino Corma*

Cite This: *ACS Catal.* 2022, 12, 4182–4193

Read Online

ACCESS | Metrics & More | Article Recommendations | Supporting Information

ABSTRACT: A heterogeneous ruthenium catalyst consisting of isolated single atoms and disordered clusters stabilized in a N-doped carbon matrix has been synthesized with very good activity and remarkable regioselectivity in the hydroformylation of 1-hexene. The role of the nitrogen heteroatoms has been probed essential to increase the catalyst stability and activity, enabling the stabilization of Ru(II)−N sites according to X-ray photoelectron spectroscopy (XPS) and XANES. Intrinsic size-dependent activity of Ru species of different atomicity has been extracted, correlating the observed reaction rate and the particle size distribution determined by means of aberration-corrected high-angle annular dark-field scanning transmission electron microscopy, permitting the identification of single-atom sites as the most active ones. This catalyst appears as a promising alternative with respect to its heterogeneous counterparts, paving the way for designing improved Ru heterogeneous catalysts.

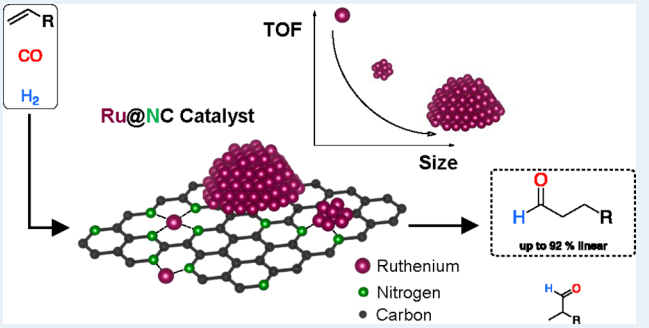

KEYWORDS: *ruthenium, hydroformylation, single site, 1-hexene, ruthenium cluster, regioselectivity*

INTRODUCTION

Hydroformylation is one of the most important C−C coupling reactions employed on an industrial scale to manufacture high-value aldehydes from syngas in a one-step process with high atom efficiency.[1,2] Regioselectivity is crucial in this process because depending on the application, linear or branched aldehydes are preferred. Particularly, when long-chain olefins are used as substrates, the linear aldehyde is the desired product either to be used directly (e.g., perfumes and flavoring agents) or as an intermediate to produce linear carboxylic acids, amines, or alcohols (detergents, plasticizers, and so on).[3] From this perspective, highly selective hydroformylation catalysts are required, and efforts have been made to control the linear versus branched isomer ratio.

The first generation of cobalt catalysts[4,5] used on an industrial scale showed modest activity under harsh operating conditions[6] and required high-purity feedstocks.[7] Later, Wilkinson developed different phosphine-modified rhodium catalysts[8,9] that improved the chemoselectivity and regioselectivity of the reaction while operating at much lower pressures than the cobalt counterpart, improving the economy of the process. A marked influence of the type of phosphine used on the rate and *n*-selectivity of the catalyst has been observed based on steric and electronic effects.[10] This leads to the development of more complex phosphine ligand-modified cobalt[11,12] and rhodium[10,13−15] catalysts, the latter being superior to cobalt for short-chain olefins feedstocks. However, the intrinsic cost of rhodium and the degradation of the phosphine ligand must be considered for the overall economics and sustainability of the process.[2] Recently, Stanley et al.[12] discovered a highly active cationic cobalt(II) biphosphine catalyst approaching the reactivity of a standard industrial $HRh(CO)(PPh_3)_2$ catalyst, with a higher isomerization rate. In this context, ruthenium has been regarded as a possible candidate to replace rhodium and cobalt on an industrial scale.[16] Despite being more abundant than rhodium, organic ligands are still required to ameliorate the catalytic properties of the ruthenium complex by reducing the undesired reduction and isomerization reaction and improving the activity toward hydroformylation.[17−19] Nevertheless, the activity of the reported Ru catalysts is relatively low, and an increase between one and two orders in activity will be required to consider Ru as an alternative to the Rh hydroformylation catalyst.[19]

Taking into account all of the above, the preparation of a ligand-free supported Rh catalyst and, even better, Ru catalyst for hydroformylation would be desirable. Unfortunately, despite major efforts being invested in developing new

Received: December 13, 2021
Revised: March 10, 2022
Published: March 23, 2022

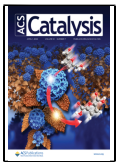

https://doi.org/10.1021/acscatal.1c05737
ACS Catal. 2022, 12, 4182−4193

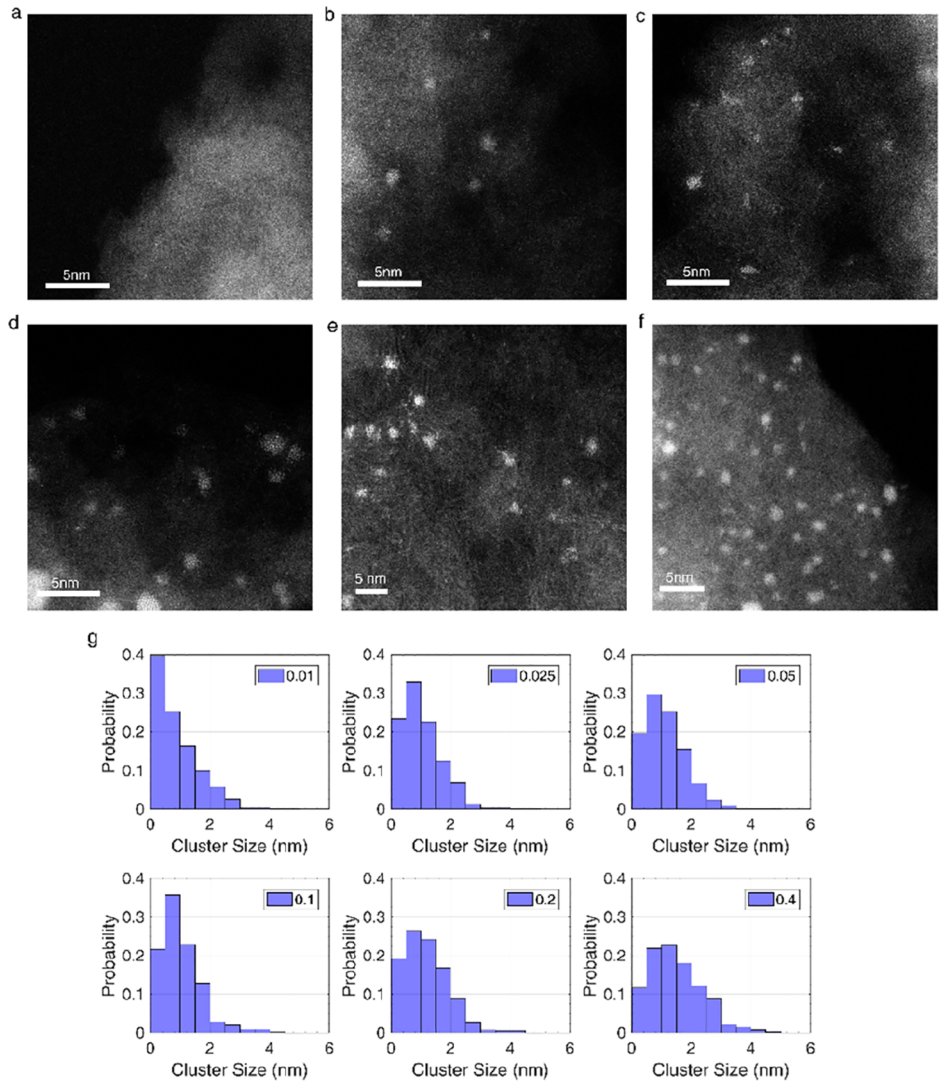

Figure 1. Aberration-corrected HAADF-STEM images under high magnification for (a) 0.0125Ru@NC, (b) 0.025Ru@NC, (c) 0.05Ru@NC, (d) 0.1Ru@NC, (e) 0.2Ru@NC, and (f) 0.4Ru@NC. (g) PSDs for the catalyst samples. Note that more than 500 particles have been measured automatically in each sample.

hydroformylation heterogeneous catalysts, moderate to poor results have been obtained up to date, and the catalysts are characterized by slow overall rates and limited regiocontrol.[20,21]

In the case of Rh metal, different approaches have been studied for the heterogenization of Rh catalysts including the direct immobilization of the complex on a solid support,[22−27] such as supporting metallic[28−30] or ligand-modified Rh nanoparticles,[31−35] immobilization in an ionic liquid phase[36−40] and, more recently, the preparation of single-atom catalysts.[41−44] Remarkable high activity and chemoselectivity have been recently reported on single-atom Rh catalysts for the hydroformylation of olefins, resulting in a promising alternative to homogeneous catalysts. In particular, single-atom Rh catalysts supported on ZnO nanowires have demonstrated activities comparable to those of a homogeneous catalyst for the hydroformylation of different substrates such as 1-hexene and styrene, albeit with low regioselectivity (n/iso = 50:50) in the case of styrene.[43] In analogy, a high turnover number (TON 1496) and high chemoselectivity (88%) and regioselectivity (n/iso = 87:13) are reported in the hydroformylation of 1-hexene on a xantphos-doped porous organic polymer containing isolated Rh atoms.[45] Unfortunately, in the case of ruthenium catalysts, the use of polymeric supports suffers from stability limitations due to the higher reaction temperatures usually required as a consequence of their lower intrinsic activity. Up to now, the best results have been observed in $[Ru(CO)_4]_n$/MWNCT systems, with TON 21, 85% chemoselectivity, and regioselectivity with n/iso = 63:27.[20]

To our knowledge, the use of single-atom Ru catalysts in the hydroformylation of olefins has not been reported yet, although if they were highly active and selective, they could represent a promising cost-efficient alternative to the present Rh catalysts.

Herein, a new type of heterogeneous ruthenium catalysts consisting of isolated single atoms (SAs) and clusters stabilized in a N-doped carbon matrix has been developed for hydroformylation of olefins. A high regioselectivity and remarkable activity, mainly ascribed to the formation of isolated Ru single sites, have been obtained operating at 40 bar, 150 °C, and CO/H_2 ratio 1:1. These results open an opportunity for supported Ru catalysts in the hydroformylation of olefins.

https://doi.org/10.1021/acscatal.1c05737
ACS Catal. 2022, 12, 4182−4193

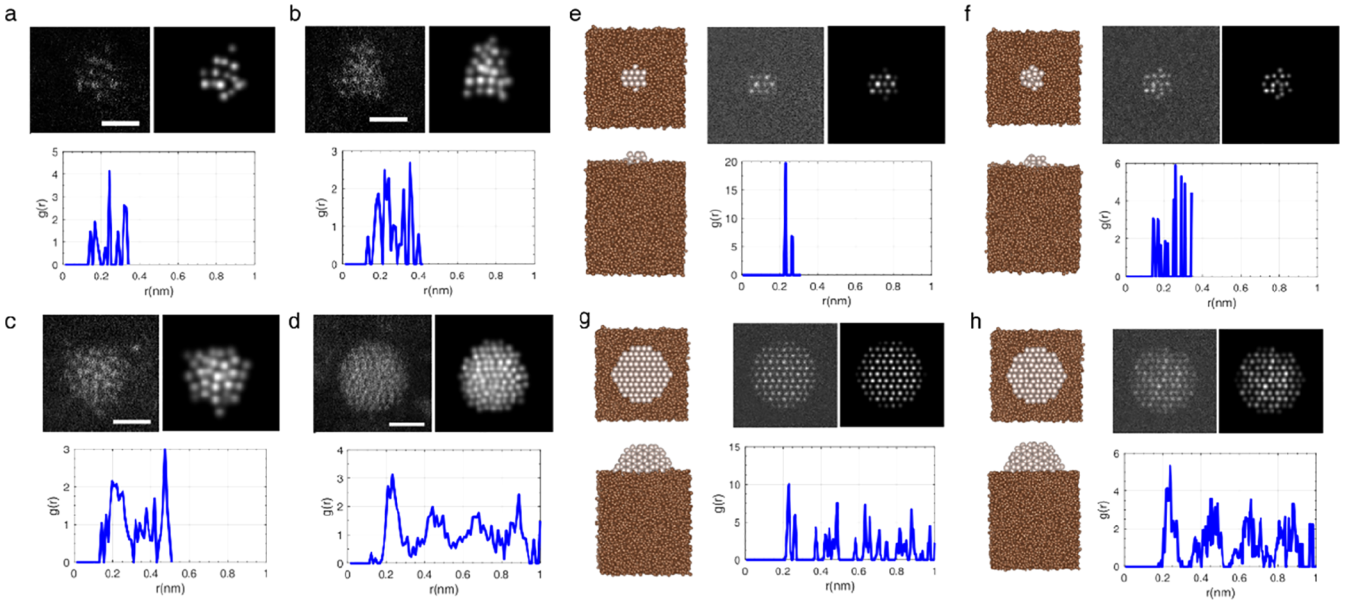

Figure 2. RDFs calculated from experimental HR-HAADF-STEM images of Ru clusters (a,b) and nanoparticles (c,d) and simulated HR HAADF-STEM images for ordered (e) and highly disordered clusters (f) and ordered (g) and slightly disordered (h) Ru nanoparticles. The profile and top views of the structural models used for the simulations are also shown.

RESULTS AND DISCUSSION

Synthesis and Characterization. Highly dispersed ruthenium species were prepared by dispersing controlled amounts of ammonium alginate (AG), 20% wt, on a carbonaceous support (Norit CN-1) and subsequent introduction of the ruthenium precursor ($RuCl_3 \cdot 3H_2O$) in alcoholic solution (1-butanol) to achieve a final Ru loading between 0.0125 and 0.4 wt %. The as-prepared samples were submitted to a pyrolysis treatment under a N_2 atmosphere at 800 °C. The pyrolyzed catalysts are denoted as *X*Ru@NC, where *X* represents the nominal weight loading of Ru used in the synthesis procedure. The amount of nitrogen, coming from the alginate precursor, is around 1 wt % in all samples. Details of the synthesis procedure and physico-chemical properties of the catalysts are included in the Experimental Section and Supporting Information. The idea behind using AG for the catalyst preparation was to generate nitrogen-containing compounds on the surface of the carbon-based support that, by interacting with Ru, could better disperse the metal, stabilizing SAs and small nanoclusters toward sintering and/or metal leaching during the reaction, while modifying the electronic characteristics of the Ru on the surface. Both effects should impact catalyst stability, activity, and selectivity.

Aberration-corrected electron microscopy revealed the existence of uniformly distributed Ru SAs in all samples, which are visualized as bright spots in the high-angle annular dark-field scanning transmission electron microscopy (HAADF-STEM) images, Figure 1. These SAs coexist with Ru in the form of small subnanometric clusters of low atomicity (~2−8 atoms and size < 1 nm), medium-size clusters (~8−33 atoms and size < 1.5 nm), and Ru nanoparticles (size >1.5 nm), Figure 1 and Supporting Information.

From the automated analysis (as described in detail in Supporting Information) of sets of HAADF-STEM images, the relative population of the different forms of Ru could be determined for all the catalysts. According to their particle size distribution (PSDs), Figure 1 shows that the percentage of isolated Ru atoms is roughly 40% for the catalyst with 0.0125 wt % Ru; around 20% for the intermediate loadings, that is, 0.025, 0.05, and 0.10 wt % Ru content; and 19−12% in the catalysts with 0.2 and 0.4 wt % of Ru, respectively. In correspondence, clusters of low and medium atomicity, with size between 0.5-1.5 nm, predominate at intermediate Ru loadings (0.02 to 0.2 wt % Ru), while the fraction of larger nanoparticles, in the 2−5 nm size range, increases when increasing metal loading, reaching around 40% for the catalyst with the highest Ru loading (0.4 wt %).

The detailed analysis of the contrasts in the atomically resolved HAADF-STEM images provide information about the structure of the different types of Ru entities, Figure 2. Denoising of the experimental HR HAADF-STEM images, using the approach described in Supporting Information and comparison with simulated ones, evidenced the disordered nature of both low-atomicity and medium-size Ru clusters, Figure 2a−c. In fact, the radial distribution functions (RDFs) obtained from the images of these entities (details in Supporting Information) depict a broad distribution of Ru−Ru projected distances in both cases, in clear contrast with that expected for a perfectly ordered cluster, Figure 2e. The most frequent Ru−Ru projected distance determined from the first broad maximum of the RDFs falls close to 2.42 Å, a value larger than that expected for the projection of the bulk structure, 2.32 Å. Moreover, the Ru−Ru projected distances observed in the experimental images span a rather wide range, from 1.4 Å up to 3.3 Å. Altogether, these results point out to structurally distorted clusters in strong interaction with N, O, and/or C atoms of the support.

The origin of bond length disorder on carbon-supported metal clusters has been widely studied in the literature using density functional theory calculations and has been associated to the combined effect of cluster shape, interfacial interaction with the support, and anisotropic relaxation within the cluster.[46] It is evident that this type of disorder is more sensitively seen in small clusters.[47] In fact, in the case of Ru nanoparticles (NPs), the analysis of the experimental results

https://doi.org/10.1021/acscatal.1c05737
ACS Catal. 2022, 12, 4182−4193

and simulated image in Figure 2d indicates that some of them retain a certain degree of structural disorder (Figure 2h and Supporting Information), with Ru−Ru distances of 1.2−3.1 Å, but the most frequent Ru−Ru distance in the NPs is 2.31 Å, much closer to that expected for the fully ordered bulk projected structure.

The potential interactions between the surface N and Ru have been studied by means of STEM−EDS analysis, X-ray photoelectron spectroscopy (XPS), and Raman spectroscopy.

First of all, STEM−EDS results (Figure S15) clearly confirm a uniform distribution of N on the support overlapping with the Ru signal. Then, in order to define the electronic properties of the ruthenium species visualized by microscopy and to define if there is an interaction with the nitrogen adatoms, XPS analysis has been carried out at the Ru $3d_{5/2}$ and N 1s core lines. The detection limit at the Ru 3d core line restricts our study to loadings above 0.1 wt % Ru. In detail, at the Ru $3d_{5/2}$ core line, ruthenium species at binding energies (BEs) of 280.1, 281.2, and 282.7 ± 0.2 eV are observed in the 0.1−0.4Ru@NC samples (Table 1, and deconvoluted spectra in Figure S22). The first component at 1 eV higher BE than that of bulk ruthenium (280.0 ± 0.5 eV)[48−51] may correspond to highly dispersed Ru^0 species and/or ruthenium atoms interacting with N, as recently reported.[52] In that work, Ru atoms interacting with N atoms embedded in a carbon matrix, characterized by ∼1 eV higher BE than that of Ru^0, have been ascribed to Ru(II) in analogy to that reported in the literature for a ruthenium trisbipyridine complex or ruthenium catalysts with nitrogen heterocyclic ligands.[53] In addition, the higher BE of 281.2 and 282.7 eV should correspond to the higher oxidation state of ruthenium [Ru(IV) and Ru(VI)], likely as ruthenium oxide clusters.[48,53,54] Parallel to these data, the interaction of Ru species with N atoms can be retrieved by careful analysis of the N 1s XPS spectra. In detail, deconvolution of the N1s core level in the studied samples (Figure S24) results in five components ascribed to pyridinic nitrogen, 398.6 eV; ruthenium-bonded nitrogen, Ru−N, 399.2 eV;[55] pyrroleic nitrogen, 400.5 eV, and graphitic N, 401.1−402.7 eV.[56−58] Furthermore, the presence of Ru−N bonds is confirmed by Raman spectroscopy, where a band at 460 cm^{-1} is observed, which has been reported in the literature as the Ru−N stretching vibration[59] (Figure S29). At this point, assuming that the XPS N 1s component at 399.2 eV is due to N adatoms in a Ru−N interaction and that the component at 280.3 ± 0.2 eV in the Ru $3d_{5/2}$ core level is associated to Ru species in the same type of interaction, it is possible to calculate the N/Ru atomic ratio by simply correlating both peak areas, providing that the contribution of highly dispersed Ru^0 nanoparticles at the 280.3 eV Ru $3d_{5/2}$ peak is minimal. By doing so, a N/Ru atomic ratio of ∼4.7 is obtained for the 0.1 Ru@NC sample. Lower values, 3 and 2.2, are obtained on the 0.2Ru@NC and 0.4Ru@NC samples, respectively, where the possible contribution of Ru^0 in the Ru $3d_{5/2}$ component at 280.3 eV affects the accuracy of the N/Ru estimation.

In accordance with the microscopy study and in good agreement with XPS data, Ru K-edge X-ray absorption spectroscopy clearly shows that the bulk of the material is dominated by single-site Ru atoms, with an average formal oxidation state[60,61] of +1.2 and an average of 3−3.7 coordinating light atoms. Although the Ru oxidation state has been extracted while analyzing the X-ray absorption near-edge region (XANES, Figure 3 left panel), details on the local structure have been obtained by fitting the extended X-ray absorption fine structure (EXAFS, Figure 3 right panels) as described in the Supporting Information. As the Ru loading in the samples increases, the Ru−Ru scattering contribution in

Table 1. XPS Values of Ru $3d_{5/2}$ BE (eV) and the Surface Composition of Selected Samples

	Ru $3d_{5/2}$ BE (eV)[a]			
sample	$Ru^{(II)}$	$Ru^{(IV,VI)}$		C/O/N/Ru[b]
0.4Ru@NC	280.1 (25%)	280.8 (29%)	282.7 (46%)	94.5/4.0/1.1/0.3
0.2Ru@NC	280.3 (21%)	281.4 (27%)	283.1 (51%)	93.3/5.5/1.0/0.2
0.1Ru@NC	280.3 (17%)	281.4 (25%)	283.0 (58%)	95.3/3.4/1.2/0.2
0.2Ru@NaC		281.3 (45%)	282.8 (55%)	C/O/Na/Ru[b] 70.5/19.2/7.8/2.6

[a]In brackets, the percentage of each species. [b]Surface atomic ratio.

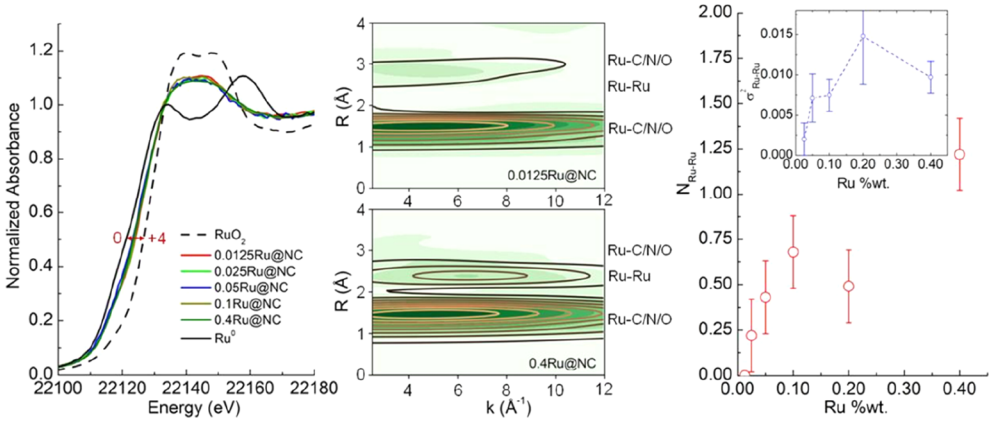

Figure 3. Ru K-edge XANES spectra of the XRu@NC catalysts compared with Ru^0 and Ru^{4+} references (left); Cauchy wavelet transform of the EXAFS signal allowing a visual deconvolution of the signal based on both bond distance (R) and the speciation of the scattering atom, showing both the data (green density) and fit model (black contour), (center); and the number of neighboring Ru atoms plotted as a function of the Ru loading (right). The inset shows the Debye-Waller value (Ru−Ru disorder parameter) as a function of the Ru loading. The Ru−Ru contribution becomes clearly visible and increases in structural disorder by increasing the Ru loading. The suppression of the long Ru−N/O/C contribution with increasing Ru clustering on the Cauchy wavelet transform maps comes from interfering and contrast effects.

https://doi.org/10.1021/acscatal.1c05737
ACS Catal. 2022, 12, 4182−4193

Table 2. Average Value and Standard Deviations of the Catalytic Results for the Different Loadings of Ru@NC[a]

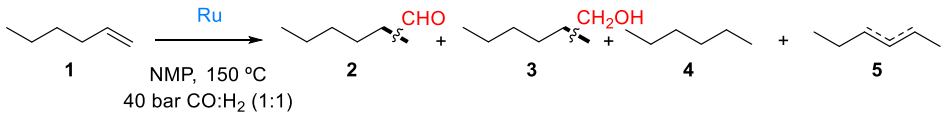

			yield (%)			
entry	sample	conv. **1** (%)	**2** (n/iso)[b]	**3** (n/iso)[b]	TON[c] (−)	TOF[d] (h^{-1})
1	$Ru_3(CO)_{12}$[e]	19.1	3.6 (75:25)	0 (−)	651.6	180.5
2	0.0125Ru@NC	15 ± 0.8	5.7 ± 0.5 (76:24)	0 ± 0 (−)	1470 ± 129	208.3 ± 3.9
3	0.0125Ru@NC[f]	43.5	11.4 (77:23)	0 (−)	1104	195.3
4	0.025Ru@NC	45.5 ± 0.5	22.3 ± 1.2 (84:16)	1.3 ± 0.5 (100:0)	2311 ± 135	182.0 ± 6.7
5	0.05Ru@NC	62.8 ± 2.6	30.2 ± 1.2 (83:17)	1.7 ± 0.5 (100:0)	1647 ± 74	147.8 ± 5.7
6	0.1Ru@NC	84.0 ± 2.9	42.7 ± 3.3 (83:17)	2.7 ± 0.9 (100:0)	1336 ± 153	154.3 ± 7.1
7	0.2Ru@NC	94.0 ± 4.3	49.3 ± 3.5 (93:7)	2.8 ± 0.8 (100:0)	757 ± 68	146.3 ± 4.3
8	0.4Ru@NC	98.3 ± 0.9	46.3 ± 2.5 (93:7)	4.3 ± 0.9 (100:0)	370 ± 20	78.3 ± 4.1
9	0.2Ru@NaC	55.5	28.4 (77:23)	0 (−)	371	92.8

[a]Reaction conditions: 3.2 mmol of 1-hexene, 0.95 mmol of cyclohexane (internal standard), 100 mg of the catalyst, 40 bar CO/H_2 (1:1), 150 °C, 750 r.p.m, and 24 h. [b]Ratio of the linear product to the branched product. [c]mmol of 1-heptanal/total mmol of Ru. [d]Rate of formation of 1-heptanal/total mmol of Ru. [e]5.7 ppm $Ru_3(CO)_{12}$; TON and TOF calculated considering all Ru as active. [f]210 mg of catalyst.

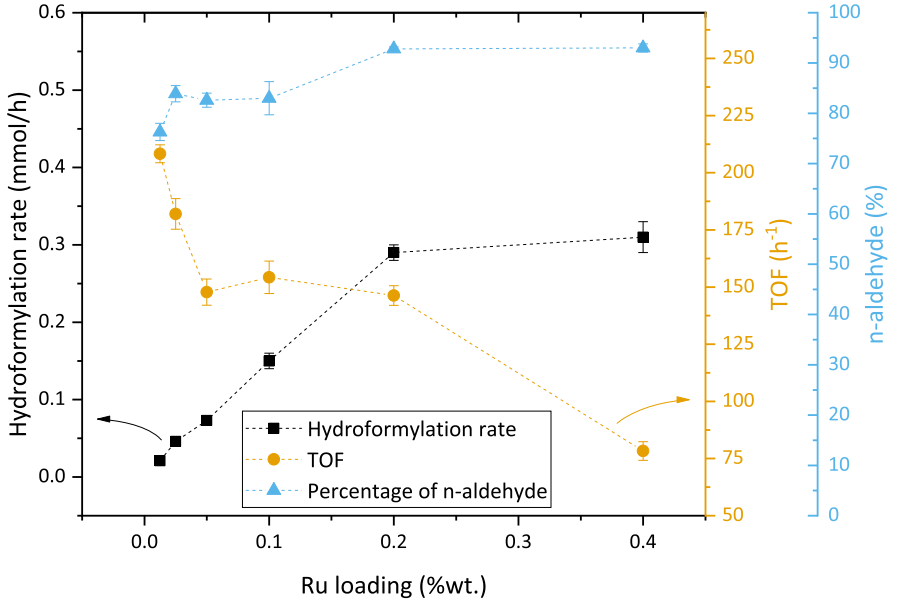

Figure 4. Representation of the catalytic data for different Ru@NC-loaded catalysts hydroformylation rate, black (left); turnover frequency (TOF), orange (assuming all metal species to be active); and percentage to the linear aldehyde (*n*-aldehyde), blue (right).

the EXAFS region increases, consistently with the formation of Ru clusters. This, together with the high Ru−Ru disorder parameter detected in the Ru clusters (inset in the Figure 3 right panel), clearly indicates the formation of small, dispersed, and highly disordered Ru clusters in the bulk, in full agreement with the microscopy data.

Catalytic Results. The catalytic performance of all the samples in the hydroformylation of 1-hexene is given in Table 2 and displayed in Figure 4. Interestingly, for all the catalysts, the hydrogenation of the olefin was almost completely inhibited without the need of additives as in the case of homogeneous catalysts (Table S31.1). On the other hand, both the conversion and regioselectivity for hydroformylation increase when the increasing ruthenium loading in the catalyst. Particularly, for the 0.2Ru@NC catalyst, a marked selectivity toward the hydroformylation of the terminal double bond was observed with a n/iso ratio of 93:7 (entry 7, Table 2). Moreover, it is possible to increase the catalyst activity while keeping the same regioselectivity by simply increasing the metal loading as observed in the 0.0125Ru@NC catalyst (entry 3, Table 2). Regarding the TOF number, calculated by dividing the initial reaction rate by the total number of Ru atoms, the highest value of ~208 h^{-1} is achieved for the catalyst with the lowest metal loading, that is, 0.0125Ru@NC (containing predominantly single-atom and low-atomicity Ru clusters), followed by a linear decrease when increasing the Ru content up to a loading of 0.05 wt % Ru. When the loading is increased further, between 0.05% and 0.2 wt % Ru, a critical point is reached with all samples displaying a similar particle size distribution, resulting in analogous activity per metal centre, ~ 150 h^{-1}. Finally, when the ruthenium loading is increased above 0.2%, a sharp decrease in activity, down to ~78 h^{-1}, is observed to be linked to the formation of NPs for the 0.4Ru@NC sample. These results indicate a strong relationship between the catalytic activity and the size of the Ru entity, and we will come back later to this for a deeper discussion.

https://doi.org/10.1021/acscatal.1c05737
ACS Catal. 2022, 12, 4182−4193

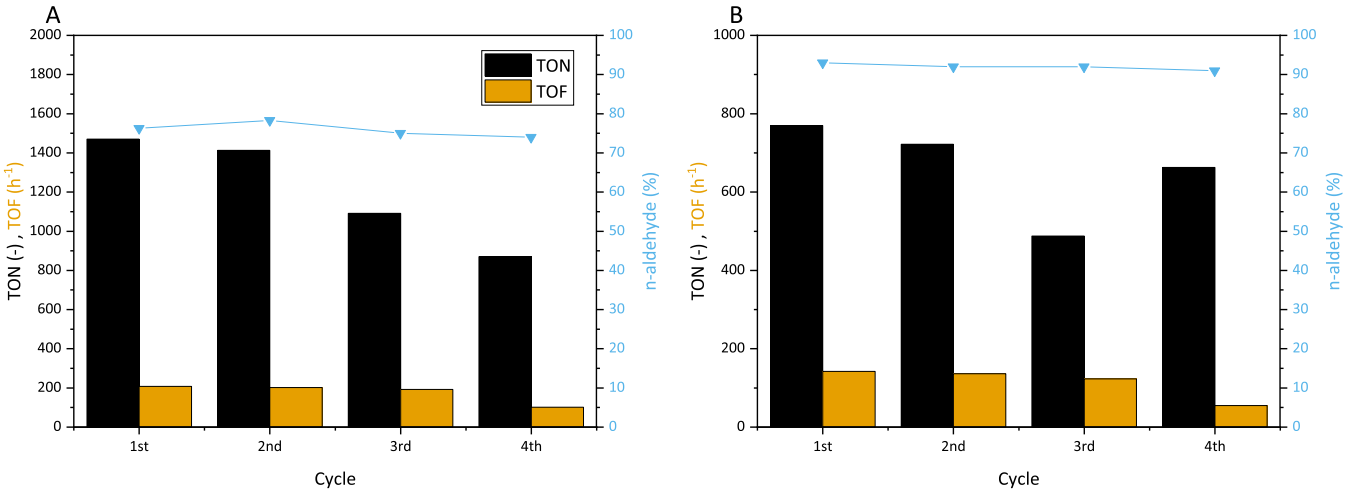

Figure 5. Representation of the most important catalytic data for each reuse of (A) 0.0125Ru@NC and (B) 0.2Ru@NC catalysts. The TON and TOF are calculated based on all metal species being equally active.

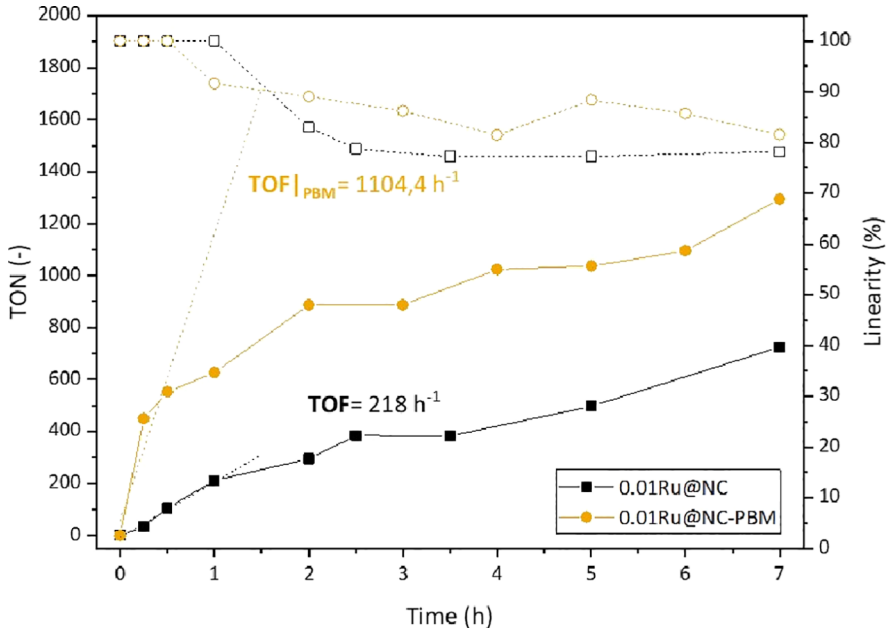

Figure 6. Effect of high-energy ball milling on the catalytic performance of the 0.01Ru@NC catalyst before (black) and after ball milling (orange). TOF is calculated based on all metal being equally active.

To study the stability of the metal species under reaction conditions, recyclability tests were performed on two representative catalysts (0.0125Ru@NC and 0.2Ru@NC). A small decrease in the activity parameters (TON and TOF) was found, but selectivity toward 1-heptanal was maintained during all recycles (Figure 5A,B). ICP-AES analysis of the reused catalyst (Table S29) shows practically no metal leaching into the liquid for the different reuses.

In addition, hot filtration experiments showed negligible activity of the liquid after removing the solid catalyst, confirming that the reaction is heterogeneously catalyzed. Micrographs of the 0.2Ru@NC catalyst after the fourth use (Figure S16) reveal the maintenance of isolated single atoms with a decrease in the percentage of clusters in favor of NPs, a behavior also supported by EXAFS. Interestingly, some ordering in the structure of metal clusters after reuse is observed in the HAADF images (Figure S17), which correlates with the clear, well-resolved feature in the Fourier transformed EXAFS spectra resulting from an increase in the Ru−Ru scattering contribution and a reduction in the Ru−Ru disorder (Tables S24 and S25). Similar to the used 0.2Ru@NC sample, the prevalence of single atoms is also observed in the used 0.0125Ru@NC sample, with a very small amount of NP formation (Figure S18).

Particularly, because the 0.0125Ru@NC catalyst after the fourth recycle shows mostly the presence of single atoms, an initial approximation to the determination of the intrinsic activity of this species could be carried out. Thus, by considering that the experimental reaction rate is only attributed to the single atom, a value of TOF_{SA} = 10 536 h^{-1} can be obtained. This first approximation can be further refined by applying a mathematical analytical method (more details in Supporting Information), considering the particle size distributions obtained from the analysis of the HR HAADF-STEM images, the ICP-AES Ru metal loading in the samples, and the initial reaction rate. By doing that, it should

https://doi.org/10.1021/acscatal.1c05737
ACS Catal. 2022, 12, 4182−4193

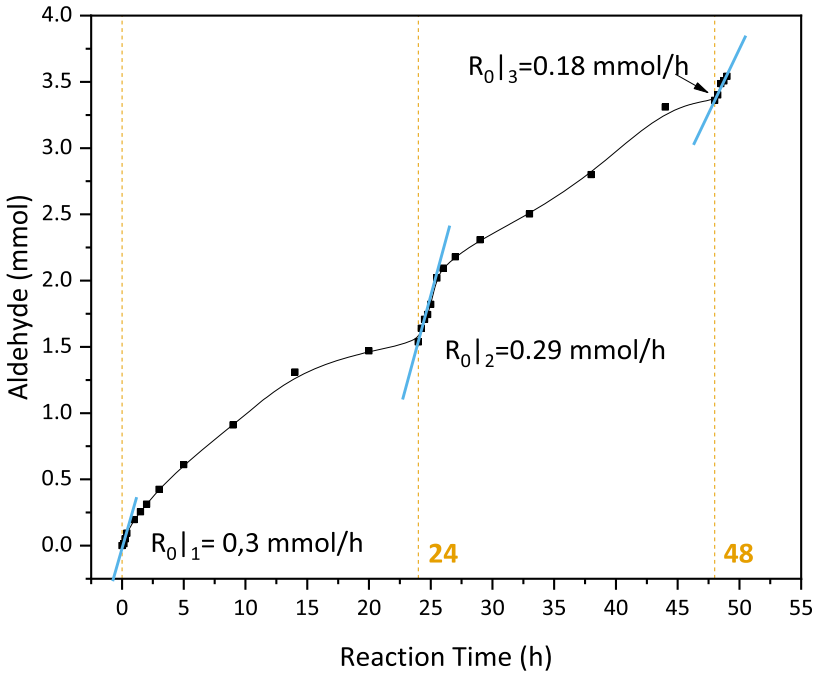

Figure 7. Kinetic data for the catalyst 0.2Ru@NC after multiple additions of 3.2 mmol of 1-hexene (dashed line) while under continuous operation with 100 mg of catalyst.

be possible to calculate the intrinsic activity of the different types of Ru entities detected in the HR HAADF-STEM images. Thus, a distribution of TOF values depending on the particle size can be achieved, resulting in a TOF of 12 000 h^{-1} for single sites (i.e., 0.25 nm), 702 h^{-1} for clusters of 1.25 nm (i.e., 33 atoms), and 10 h^{-1} for nanoparticles >1.25 nm. Based on it, the TOF values reported in Table 2 can be understood on the basis of heterogeneity of Ru species in the samples. Thus, the formation of bigger NPs with lower intrinsic activity and low surface−bulk atom ratios, contributing substantially to the catalyst metal loading, has a large negative impact on the calculated TON and TOF when considering all the metal atoms present in the catalyst, regardless of the metal crystallite size.

Nevertheless, we have also considered that, due to the nature of the pyrolysis treatment, a high amount of the loaded ruthenium metal could be occluded inside the carbonaceous matrix. Indeed, an XPS depth profile study of the catalysts showed that an important fraction of the ruthenium metal is trapped inside the carbon support (Figure S25), decreasing the amount of accessible sites. This feature also contributes to the discrepancy between the theoretical TOF values and the ones included in Table 2. High-energy ball milling has been proven to be a useful tool to modify the textural properties of different carbon-based materials[62] contributing to the breakdown of bigger agglomerates into smaller particles[62] and exposing previously occluded metal. Supported by these findings, the 0.01Ru@NC was selected and subjected to ball milling, and the milled catalyst was denoted as 0.01Ru@NC-PBM. Interestingly, the catalytic activity after ball milling increased by a factor of more than 3 (Figure 6) in accordance with a higher fraction of surface ruthenium species being determined in the depth profile XPS analysis (Figure S27).

Next, the activity of the herein reported catalysts has been compared with that of a reference homogeneous trinuclear carbonyl ruthenium cluster, $Ru_3(CO)_{12}$ (Table 1, entry 1), under the same reactions conditions with an equivalent Ru concentration as the 0.0125Ru@NC test. Notice that the heterogeneous catalyst gives similar TOF, slightly higher chemoselectivity to the aldehyde, and regioselectivity to the linear isomer under identical reaction settings. Furthermore, comparison with state of the art Ru homogeneous catalysts is given in Table S31.1, where both the $RuCl_2(PPh_3)_3$ biphenphos and the $Ru_3(CO)_{12}$-imidazoyl-substituted monophosphine system showed remarkable activities [TOF 360 and 2040 h^{-1} and 15 000 and 800 TON, respectively, albeit with other substrates (undec-10-enenitrile and 1-octene)].[63,64] However, these catalytic systems required the use of complex compounds with intricate synthesis steps, leading to very expensive ligands and were operated under different reaction conditions (higher pressures and the use of co-additives) or using dissimilar substrates. Considering heterogeneous Ru catalysts, the Ru@NC catalysts used herein exhibit markedly higher activity than that of previously reported catalysts (see Table S31.2 for state of the art catalysts), accompanied by a noteworthy superior linear to branch regioselectivity. In particular, the TOF of the Ru single atoms (12 000 h^{-1}) in the Ru@NC catalyst, as per the calculations described above, is between one and two orders of magnitude higher than the actual reported Ru catalysts.

From the point of view of potential application in a semicontinuous operation mode, an additional experiment has been carried out by consecutive additions of 1-hexene charges into the batch reactor. As visualized in Figure 7 in the case of the 0.2Ru@NC sample, the aldehyde production rate remained constant, allowing long-term operation without any apparent sign of catalyst deactivation.

As we said before, our original hypothesis was that the surface N, by interacting with Ru, should stabilize and change the electronic properties of the Ru atoms. Indeed, when Ru was supported on the same carbon support (Norit CN-1) in the absence of the nitrogen precursor (0.2Ru@NaC sample,

https://doi.org/10.1021/acscatal.1c05737
ACS Catal. 2022, 12, 4182−4193

Table 3. Catalytic Results for the Hydroformylation of Different Substrates with the 0.2Ru@NC Catalyst[a]

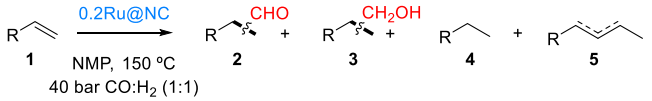

			yield (%)					
entry	substrate	conv. 1 (%)	2 (n/iso)[b]	3 (n/iso)	4	5	TON[c] (−)	TOF[d] (h^{-1})
1	1-pentene	80	39 (93:07)	<1 (−)	2	30	564	90
2	1-hexene	100	54 (92:08)	3 (100:0)	3	42	862	153
4	*cis*-2-hexene	66	9 (81:19)	1 (100:0)	1	55	110	20
5	*trans*-2-hexene	70	8 (82:18)	2 (100:0)	1	56	86	25
7	1-octene	94	38 (92:8)	3 (97:3)	3	49	650	111
8	1-nonene	92	37 (87:13)	5 (90:10)	2	46	521	97
9	1-decene	91	44 (90:10)	3 (96:4)	3	43	691	102
10	cyclohexene[e]	27	25 (−)	0 (−)	2		398	136
11	styrene	80	7 (80:20[f]	0 (−)	33		111	35

[a]Reaction conditions: 3.2 mmol of substrate, 0.95 mmol of cyclohexane (internal standard), 100 mg of the catalyst, 40 bar CO/H_2 (1:1), 150 °C, 750 r.p.m, and 24 h. [b]Ratio of the linear product to the branched product. [c]mmol of 1-heptanal/total mmol of Ru. [d]Rate of formation of 1-heptanal/total mmol of Ru. [e]0.95 mmol of heptane as an internal standard. [f]Additional formation of insoluble oligomers as byproducts.

details in Supporting Information), the initial rate of the reaction was 91 versus 147 h^{-1} of the 0.2Ru@NC sample (Figure S32). More importantly, the rate of the reaction on 0.2Ru@NaC strongly declines with reaction time, along with the relatively large amount of leached species in the liquid and a marked decrease in Ru in the solid sample. Furthermore, the regioselectivity in this sample is significantly lower than that with the 0.2Ru@NC catalyst (n: iso ratio of 77:23 versus 93:7, respectively, entry 9 and 7 in Table 2) and similar to that observed with the homogeneous $Ru_3(CO)_{12}$ sample (Table 2, entry 1). In fact, hot filtration experiments performed after 1 h of reaction lead to a complete loss of catalytic activity in the solid after filtration, while the solution remains active, revealing that the activity can be ascribed to the metal species in solution (Figure S34). So far, combining catalytic with spectroscopic data, we can postulate single-ruthenium sites as the most active ones, which according to XPS data may correspond to Ru−N entities, where Ru may appear as Ru(II) in a N/Ru coordination shell of ∼4.5. Clusters of higher atomicity are less active, appearing in an oxygen environment likely as oxidized species. The fact that the Ru species appear in different electronic states explains their markedly different intrinsic activity. Finally, the activity of NPs is negligible, and their presence reduces strongly the global activity of the catalyst.

Considering the very good catalytic performance of the Ru@NC samples prepared herein, other substrates were explored. Results, included in Tables 3 and S27, confirmed in all cases excellent activity, chemoselectivity, and regioselectivity for a variety of olefins.

CONCLUSIONS

In conclusion, isolated single Ru atoms and clusters have been efficiency stabilized on a N-doped carbon-base Ru@NC catalyst, using a simple environmentally friendly and cost-efficient synthetic method. The synthesized catalyst shows competitive catalytic activity compared to the state of the art Ru-supported catalysts in the hydroformylation of olefins with a high regioselectivity (n/iso = 93:7) and stability under continuous operating conditions. By means of aberration-corrected HR-STEM images correlated with initial reaction rates, size-dependent TOF values have been calculated, with the highest TOF value attributed to single atoms, exhibiting a high activity (TOF 12 000 h^{-1}). This active site has been identified as Ru(II)−N species, which remain stable without sintering after sequential catalyst cycles. Lower TOF values have been calculated for Ru clusters of higher atomicity, and NPs show a very low intrinsic activity. The role of nitrogen has been proven essential for both the generation of the active site and their stabilization under reaction conditions. Thus, the very good regioselectivity and activity of single Ru atoms in the hydroformylation of olefins represent an interesting atom-efficient and economical alternative to be further studied.

EXPERIMENTAL SECTION

Synthesis of *X*Ru@NC. The catalysts were prepared by dispersing controlled amounts of AG on a carbonaceous support and subsequent introduction of the ruthenium precursor in alcoholic solution.[65,66] Typically, for 1 g of catalyst, 200 mg of alginic acid (HAG, Sigma-Aldrich) was dispersed in 20 mL of MiliQ water to obtain the desired alginate loading. Then, the acid was transformed into the more soluble ammonium salt by slow addition of 2 mL of NH_4OH (Sigma Aldrich, 28%) until slightly basic pH. The activated carbon support Norit CN-1 (Sigma-Aldrich), 800 mg, was added, and the mixture was stirred for 1 h. Water was eliminated under reduced pressure at 65 °C, and the dried solids were ground until a fine powder was obtained. The obtained dried support (AG/C) was added to 10 mL of 1-butanol, containing the desired amount of $RuCl_3{\cdot}xH_2O$ (Johnson Matthey, 40%), and kept at the reflux temperature (117.7 °C) of the corresponding alcohol for 16 h. The Ru-containing solid sample was filtered, washed three times with 50 mL of ethanol, and dried in vacuo overnight. Finally, the as-prepared sample was submitted to a pyrolysis treatment at a low rate 50 mL/min N_2 at 800 °C for 2 h with a heating rate of 25 °C/min. The catalysts were labeled *X*Ru@NC, where *X* is the ruthenium loading in wt %.

Synthesis of 0.2Ru@NaC. A similar process as for the nitrogen-doped carbon catalyst was performed, the only difference being the use of sodium alginate instead of AG. In this case, 0.2 g of sodium alginate (NaAG) was dissolved in 20 mL of miliQ water. The mixture was stirred for 2 h at room temperature until the complete dissolution of the sodium

https://doi.org/10.1021/acscatal.1c05737
ACS Catal. 2022, 12, 4182−4193

alginate salt, and then, 800 mg of Norit CN-1 carbon was added and exactly the same steps as the ones described for the 0.2Ru@NC catalyst were repeated.

High-Energy Wet Ball Milling. The catalysts were milled in a Retsch PM100 planetary ball mill using steel balls. 300 mg of the 0.01Ru@NC catalyst was added to the milling jar and milled for 2 h at 400 r.p.m, yielding the powder denoted as 0.01Ru@NC-PBM.

Catalyst Characterization. The Ru content was analyzed by energy-dispersive X-ray fluorescence (EDXRF) employing a PANalytical MiniPal4 spectrometer and inductively coupled plasma-optical emission spectroscopy (ICP-OES, iCAP PRO spectrometer, Thermo Scientific). Thermogravimetric analysis (TGA and DTG) was conducted to determine the AG content and study the transformation during the pyrolysis process. TGA and DTG were carried out under a nitrogen flow with a NETZSCH STA 449 F3 Jupiter analyzer. The range of temperature was 25 to 800 °C with a heating rage of 10 °C·min^{-1}. The samples were measured as prepared without any pre-treatment. The nitrogen content was studied by elemental analysis. The analysis was conducted using an EA−1108 (Fisons) element analyzer. Sulfanilamide was used as a reference pattern.

HAADF-STEM was performed on a double-aberration-corrected, monochromated, Titan[3] Themis 60−300 microscope working at 200 kV at the Servicios Centrales de Investigación Científica y Tecnológica (DME SC-ICYT), University of Cádiz, Spain. The aberrations of the condenser lenses were corrected up to fourth order using the Zemlin tableau to obtain a sub-Angstrom electron probe. A condenser aperture of 50 μm yielding an electron probe with a convergence angle of 18 mrad was used, and the annular dark-field (ADF) collection angle ranged from 41 to 198 mrad. The structural models used in the HR-HAADF image simulation studies were built with RHODIUS, a computer program developed at Cadiz University. TEMSIM software was used to calculate the HR-HAADF images from these models. XEDS acquisitions were performed using a SuperX G2 detector. In order to get a high signal-to-noise ratio, a beam current of 0.08 nA and a dwell pixel time of 100 μs were used, which resulted in a total acquisition time of 5s per frame, recording a total of 240 frames. To extract XEDS elemental maps, the C K, N K, and Ru L family lines were used. The XEDS elemental maps were post-filtered using a 3 × 3 pixel average to improve the visualization.

Ru K-edge X-ray absorption spectra (XAS) were acquired at room temperature over boron-diluted samples in the form of pellets. XAS spectra were collected in the fluorescence mode employing a Si311 double-crystal monochromator and a six-channel multi-element SDD detector available at the CLAESS beamline[67] of the ALBA synchrotron. Several XAS repeats were collected to ensure reproducibility and statistics. The averaged spectra were treated using the Athena software package.[68] The energy scale was calibrated by setting the first inflection point of the Ru metal spectra at 22 117 eV. EXAFS was extracted using the autobk algorithm employing a spline in the 0 to 14.5 Å^{-1} region of k-space having an R_{bkg} of 1. The FEFF6 code[68,69] was used for scattering path generation, and multi (k^1, k^2, k^3)-weighted fits of the data were carried out in r-space over an r-range of 1.0−3.2 Å and a k-range of 2.5−12 Å^{-1}. The $S_0{}^2$ value was set to 0.9, and a global E_0 was employed with the initial E_0 value set to the first inflection point of the rising edge. Single-scattering paths were fit in terms of a Δreff and σ^2, which represent the deviation from the expected interatomic distances and the structural disorder, respectively. Initial values of 0 Å for Δreff and 0.003 Å^{-1} for σ^2 were employed to explore Ru−C/N/O interactions with interatomic distances of 2.05, 2.67, 3.40 Å and Ru−Ru interactions with interatomic distances of 2.67 and 3.40 Å. To assess the goodness of the fits, both the R_{factor} (% R) and the reduced χ^2 ($\chi_v{}^2$) were minimized, ensuring that the data were not over-fitted. An increase in the number of variables is generally expected to improve the R_{factor}; however, $\chi_v{}^2$ may go through a minimum and then increase, which is an indication that the model is over-fitting the data.[70] Best fit models were determined using a grid search with fixed values for path coordination numbers (N) by employing Larch, the Python implementation of Artemis.[71,72]

The surface composition and the chemical state of ruthenium and nitrogen were determined by XPS. Photoelectron spectra were recorded with a PHOIBOS 150 MCD 9 analyzer from SPECS and a monochromatic Alkα X-ray energy of 1486.60 eV under vacuum conditions (10^{-9}mbar) and 25 °C. The relative quantification of Ru, C, O, and N has been carried out using casa XPS software. BE has been corrected to C1s at 284.5 eV. Depth profile XPS studies were carried out at the NAPP end station of CIRCE BL24 at the ALBA Synchrotron light source facility using X-ray energies of 500, 850, and 1400 eV, allowing probing sample depth of 1.6, 2.8, and 4.6 nm, respectively. The probing depth was calculated using QUASES-IMFP-TPP2M software.

Hydroformylation Catalytic Test. 1-hexene was used as model reaction substrate. The reaction was carried out in a stainless-steel autoclave reactor equipped with a PEEK (polyether ether ketone) liner. The autoclave was modified to allow for sample extraction under high pressure. In a typical experiment, 100 mg of the catalyst, 2 mL of N-methyl pyrrolidone (NMP), 80 mg of cyclohexane (0.95 mmol, as an internal standard), and 270 mg of 1-hexene (3.2 mmol) were added in quick succession to minimize errors by evaporation. The reactor was sealed and purged three times at 10 bar with the syngas reaction mixture (CO/H_2 ratio 1:1) and pressurized to 40 bar. Finally, the autoclave was heated to 150 °C. Conversion and yield were determined by gas chromatography. Gas chromatography was performed with a Varian 3900 apparatus equipped with an HP-5 column (5% phenyl, 95% methylpolysiloxane, 30 m, and 0.25 mm × 0.25 μm). The identification of the products was performed by GC−MS analyses on an Agilent spectrometer equipped with the same column as a chromatograph and operated under the same conditions. Studies using different types of solvents have been carried out, and their results are included in the Supporting Information, in Section 3, Table S28.

■ ASSOCIATED CONTENT

Supporting Information

The Supporting Information is available free of charge at https://pubs.acs.org/doi/10.1021/acscatal.1c05737.

Materials and methods, physico-chemical properties of Ru@NC catalysts (chemical composition analysis, textural properties, HAADF-STEM, XPS, Raman spectroscopy, and XAS), catalytic results (hot filtration: leaching test and homogeneous experiments), and summary of the ruthenium state of the art catalyst (PDF)

https://doi.org/10.1021/acscatal.1c05737
ACS Catal. 2022, 12, 4182−4193

AUTHOR INFORMATION

Corresponding Author

Avelino Corma − *Instituto de Tecnología Química, Universitat Politècnica de València-Consejo Superior de Investigaciones Científicas (UPV-CSIC), 46022 Valencia, Spain;* orcid.org/0000-0002-2232-3527; Email: acorma@itq.upv.es

Authors

Francisco Javier Escobar-Bedia − *Instituto de Tecnología Química, Universitat Politècnica de València-Consejo Superior de Investigaciones Científicas (UPV-CSIC), 46022 Valencia, Spain*

Miguel Lopez-Haro − *Departamento de Ciencia de los Materiales e Ingeniería Metalúrgica y Química Inorgánica, Facultad de Ciencias, Universidad de Cádiz, Puerto Real 11510 Cádiz, Spain;* orcid.org/0000-0003-2560-8015

Jose Juan Calvino − *Departamento de Ciencia de los Materiales e Ingeniería Metalúrgica y Química Inorgánica, Facultad de Ciencias, Universidad de Cádiz, Puerto Real 11510 Cádiz, Spain;* orcid.org/0000-0002-0989-1335

Vlad Martin-Diaconescu − *CELLS—ALBA Synchrotron Radiation Facility, 08290 Cerdanyola del Vallès, Spain*

Laura Simonelli − *CELLS—ALBA Synchrotron Radiation Facility, 08290 Cerdanyola del Vallès, Spain;* orcid.org/0000-0001-5331-0633

Virginia Perez-Dieste − *CELLS—ALBA Synchrotron Radiation Facility, 08290 Cerdanyola del Vallès, Spain*

Maria J. Sabater − *Instituto de Tecnología Química, Universitat Politècnica de València-Consejo Superior de Investigaciones Científicas (UPV-CSIC), 46022 Valencia, Spain;* orcid.org/0000-0001-5089-7264

Patricia Concepción − *Instituto de Tecnología Química, Universitat Politècnica de València-Consejo Superior de Investigaciones Científicas (UPV-CSIC), 46022 Valencia, Spain;* orcid.org/0000-0003-2058-3103

Complete contact information is available at: https://pubs.acs.org/10.1021/acscatal.1c05737

Notes

The authors declare no competing financial interest.

ACKNOWLEDGMENTS

The research leading to these results has received funding from the Spanish Ministry of Science, Innovation and Universities, through the "Severo Ochoa" Excellence Programme (SEV-2016-0683) and RTI2018-099668-B-C21 and PGC2018-101247-B-100 "Programa Estatal de Generación de Conocimiento". P.C acknowledges the financial support from the "Generalitat Valenciana" through the project AICO/2020/205. HR-HAADF-STEM measurements were performed at the DME-UCA node of ELECMI ICTS with financial support from FEDER/MINECO (MAT2017-87579-R and PID2019-110018GA-I00); XAS experiments were performed at the BL22-CLÆSS beamline at the ALBA Synchrotron with the collaboration of ALBA staff as part of projects 2019093692 and 2020024106. XPS experiments were performed at the BL24-CIRCE beamline at the ALBA Synchrotron with the collaboration of ALBA staff. J.E.B acknowledges the Polytechnical University of Valencia for the economic support through the grant of an FPI scholarship associated with the PAID programme "Programa de Ayudas de Investigación y Desarrollo".

REFERENCES

(1) Linear Alpha-Olefins - Chemical Economics Handbook (CEH) | IHS Markit https://ihsmarkit.com/products/linear-alpha-olefins-chemical-economics-handbook.html (accessed Apr 28, 2020).

(2) Franke, R.; Selent, D.; Börner, A. Applied Hydroformylation. *Chem. Rev.* **2012**, *112*, 5675−5732.

(3) Herwig, J.; Fischer, R. *Aqueous Biphasic Hydroformylation BT—Rhodium Catalyzed Hydroformylation*; Van Leeuwen, P. W. N. M., Claver, C., Eds.; Springer Netherlands: Dordrecht, 2002; pp 189−202.

(4) Roelen, O. Production of Oxygenated Carbon Compounds. U.S. Patent 2,327,066 A, 1943, 17 August 1943.

(5) Roelen, O. To Chemische Verwertungsgesellschaft Oberhausen m.b.H. Verfahren zur Herstellung von sauerstoffhaltigen Verbindungen German Patent DE 849548 C, 1938/1952; U.S. Patent 2,327,066 A, 1943; Chem. Abstr. 1944, 38, 3631.

(6) Herrmann, W. A.; Cornils, B. Introduction. In *Applied Homogeneous Catalysis with Organometallic Compounds*; Wiley, 2017; pp 1−22.

(7) Canell, L. G.; Slaugh, L. H.; Mullineaux, R. D. Process for the production of aldehydes and / or alcohols by the oxo synthesis. German Patent DE 1186455 B, 1965; Chem. Abstr. 1965, 62, 90291.

(8) Osborn, J. A.; Wilkinson, G.; Young, J. F. Mild Hydroformylation of Olefins Using Rhodium Catalysts. *Chem. Commun.* **1965**, 17.

(9) Evans, D.; Osborn, J. A.; Wilkinson, G. Hydroformylation of Alkenes by Use of Rhodium Complex Catalysts. *J. Chem. Soc. A* **1968**, 3133−3142.

(10) Cornils, B.; Börner, A.; Franke, R.; Zhang, B.; Wiebus, E.; Schmid, K. Hydroformylation. In *Applied Homogeneous Catalysis with Organometallic Compounds*; Wiley, 2017; pp 23−90.

(11) Slaugh, L. H.; Mullineaux, R. D. Novel Hydroformylation Catalysts. *J. Organomet. Chem.* **1968**, *13*, 469−477.

(12) Hood, D. M.; Johnson, R. A.; Carpenter, A. E.; Vinyard, D. J.; Stanley, G. G.; Stanley, G. G. Highly Active Cationic Cobalt(II) Hydroformylation Catalysts. *Science* **2020**, *367*, 542−548.

(13) Kohlpaintner, C. W.; Fischer, R. W.; Cornils, B. Aqueous Biphasic Catalysis: Ruhrchemie/Rhône-Poulenc Oxo Process. *Appl. Catal., A* **2001**, *221*, 219−225.

(14) Jiao, Y.; Torne, M. S.; Gracia, J.; Niemantsverdriet, J. W. H.; van Leeuwen, P. W. N. M. Ligand Effects in Rhodium-Catalyzed Hydroformylation with Bisphosphines: Steric or Electronic? *Catal. Sci. Technol.* **2017**, *7*, 1404−1414.

(15) *Rhodium Catalyzed Hydroformylation*, 1st ed.; Van Leeuwen, P. W. N. M., Claver, C., Eds.; Catalysis by Metal Complexes; Springer Netherlands: Dordrecht, 2002; Vol. *22*.

(16) Evans, D.; Osborn, J. A.; Jardine, F. H.; Wilkinson, G. Homogeneous Hydrogenation and Hydroformylation Using Ruthenium Complexes. *Nature* **1965**, *208*, 1203−1204.

(17) Takahashi, K.; Yamashita, M.; Tanaka, Y.; Nozaki, K. Ruthenium/C 5 Me 5 /Bisphosphine- or Bisphosphite-Based Catalysts for Normal -Selective Hydroformylation. *Angew. Chem., Int. Ed.* **2012**, *51*, 4383−4387.

(18) Takahashi, K.; Yamashita, M.; Ichihara, T.; Nakano, K.; Nozaki, K. High-Yielding Tandem Hydroformylation/Hydrogenation of a Terminal Olefin to Produce a Linear Alcohol Using a Rh/Ru Dual Catalyst System. *Angew. Chem., Int. Ed.* **2010**, *49*, 4488−4490.

(19) Pospech, J.; Fleischer, I.; Franke, R.; Buchholz, S.; Beller, M. Alternative Metals for Homogeneous Catalyzed Hydroformylation Reactions. *Angew. Chem., Int. Ed.* **2013**, *52*, 2852−2872.

(20) Oresmaa, L.; Moreno, M. A.; Jakonen, M.; Suvanto, S.; Haukka, M. Catalytic Activity of Linear Chain Ruthenium Carbonyl Polymer $[Ru(CO)_4]_n$ in 1-Hexene Hydroformylation. *Appl. Catal., A* **2009**, *353*, 113−116.

https://doi.org/10.1021/acscatal.1c05737
ACS Catal. 2022, 12, 4182−4193

(21) Kontkanen, M.-L.; Haukka, M. Microencapsulated Ruthenium Catalyst for the Hydroformylation of 1-Hexene. *Catal. Commun.* **2012**, *23*, 25−29.
(22) Ichikawa, M. Catalytic Hydroformylation of Olefins over the Rhodium, Bimetallic RhCo, and Cobalt Carbonyl Clusters Supported with Some Metal Oxides. *J. Catal.* **1979**, *59*, 67−78.
(23) Fukuoka, A.; Rao, L.-F.; Kosugi, N.; Kuroda, H.; Ichikawa, M. Selective Hydroformylation of Ethene and Propene Catalysed on Nay Zeolite-Entrapped Rh_6 and Bimetallic RhFe Clusters and Their Structural Characterization by Extended x-Ray Absorption Fine Structure and Fourier Transform Infrared Spectroscopy. *Appl. Catal.* **1989**, *50*, 295−301.
(24) Ichikawa, M.; Rao, L.-F.; Kimura, T.; Fukuoka, A. Heterogenized Bimetallic Clusters: Their Structures and Bifunctional Catalysis. *J. Mol. Catal.* **1990**, *62*, 15−35.
(25) Huang, L.; Xu, Y.; Guo, W.; Liu, A.; Li, D.; Guo, X. Study on Catalysis by Carbonyl Cluster-Derived SiO_2-Supported Rhodium for Ethylene Hydroformylation. *Catal. Lett.* **1995**, *32*, 61−81.
(26) Huang, L.; Xu, Y.; Piao, G.; Liu, A.; Zhang, W. Enhancement of Olefin Hydroformylation Related to Supported Bimetallic Rh-Co Clusters. *Catal. Lett.* **1994**, *23*, 87−95.
(27) Huang, L. Formation of Bimetallic $RhCo_3$ Clusters from Monometallic Carbonyl Clusters on SiO_2 as Probed by Hydroformylation. *J. Mol. Catal. A: Chem.* **1997**, *125*, 47−52.
(28) Chuang, S. S. C.; Pien, S.-I. Infrared Spectroscopic Studies of Ethylene Hydroformylation on Rh/SiO_2: An Investigation of the Relationships between Homogeneous and Heterogeneous Hydroformylation. *J. Mol. Catal.* **1989**, *55*, 12−22.
(29) Chuang, S.; Pien, S. I. Infrared Study of the CO Insertion Reaction on Reduced, Oxidized, and Sulfided Rh/SiO_2 Catalysts. *J. Catal.* **1992**, *135*, 618−634.
(30) McClure, S. M.; Lundwall, M. J.; Goodman, D. W. Planar Oxide Supported Rhodium Nanoparticles as Model Catalysts. *Proc. Natl. Acad. Sci.* **2011**, *108*, 931−936.
(31) Yan, L.; Ding, Y. J.; Zhu, H. J.; Xiong, J. M.; Wang, T.; Pan, Z. D.; Lin, L. W. Ligand Modified Real Heterogeneous Catalysts for Fixed-Bed Hydroformylation of Propylene. *J. Mol. Catal. A: Chem.* **2005**, *234*, 1−7.
(32) Kim, T.; Celik, F. E.; Hanna, D. G.; Shylesh, S.; Werner, S.; Bell, A. T. Gas-Phase Hydroformylation of Propene over Silica-Supported PPh_3-Modified Rhodium Catalysts. *Top. Catal.* **2011**, *54*, 299−307.
(33) Shylesh, S.; Hanna, D.; Mlinar, A.; Kŏng, X.-Q.; Reimer, J. A.; Bell, A. T. In Situ Formation of Wilkinson-Type Hydroformylation Catalysts: Insights into the Structure, Stability, and Kinetics of Triphenylphosphine- and Xantphos-Modified Rh/SiO2. *ACS Catal.* **2013**, *3*, 348−357.
(34) Li, X.; Ding, Y.; Jiao, G.; Li, J.; Lin, R.; Gong, L.; Yan, L.; Zhu, H. A New Concept of Tethered Ligand-Modified Rh/SiO_2 Catalyst for Hydroformylation with High Stability. *Appl. Catal., A* **2009**, *353*, 266−270.
(35) Liu, J.; Yan, L.; Ding, Y.; Jiang, M.; Dong, W.; Song, X.; Liu, T.; Zhu, H. Promoting Effect of Al on Tethered Ligand-Modified Rh/SiO_2 Catalysts for Ethylene Hydroformylation. *Appl. Catal., A* **2015**, *492*, 127−132.
(36) Riisagera, A.; Fehrmanna, R.; Haumannb, M.; Wasserscheidb, P. Supported Ionic Liquids: Versatile Reaction and Separation Media. *Top. Catal.* **2006**, *40*, 91−102.
(37) Riisager, A.; Fehrmann, R.; Haumann, M.; Wasserscheid, P. Supported Ionic Liquid Phase (SILP) Catalysis: An Innovative Concept for Homogeneous Catalysis in Continuous Fixed-Bed Reactors. *Eur. J. Inorg. Chem.* **2006**, *2006*, 695−706.
(38) Haumann, M.; Riisager, A. Hydroformylation in Room Temperature Ionic Liquids (RTILs): Catalyst and Process Developments. *Chem. Rev.* **2008**, *108*, 1474−1497.
(39) Van Doorslaer, C.; Wahlen, J.; Mertens, P.; Binnemans, K.; De Vos, D. Immobilization of Molecular Catalysts in Supported Ionic Liquid Phases. *Dalton Trans.* **2010**, *39*, 8377−8390.
(40) Steinrück, H.-P.; Libuda, J.; Wasserscheid, P.; Cremer, T.; Kolbeck, C.; Laurin, M.; Maier, F.; Sobota, M.; Schulz, P. S.; Stark, M. Surface Science and Model Catalysis with Ionic Liquid-Modified Materials. *Adv. Mater.* **2011**, *23*, 2571−2587.
(41) Wang, L.; Zhang, W.; Wang, S.; Gao, Z.; Luo, Z.; Wang, X.; Zeng, R.; Li, A.; Li, H.; Wang, M.; Zheng, X.; Zhu, J.; Zhang, W.; Ma, C.; Si, R.; Zeng, J. Atomic-Level Insights in Optimizing Reaction Paths for Hydroformylation Reaction over Rh/CoO Single-Atom Catalyst. *Nat. Commun.* **2016**, *7*, 14036.
(42) Alvarado Rupflin, L.; Boscagli, C.; Schunk, S. A. Platinum Group Metal Phosphides as Efficient Catalysts in Hydroprocessing and Syngas-Related Catalysis. *Catalysts* **2018**, *8*, 122.
(43) Lang, R.; Li, T.; Matsumura, D.; Miao, S.; Ren, Y.; Cui, Y.-T.; Tan, Y.; Qiao, B.; Li, L.; Wang, A.; Wang, X.; Zhang, T. Hydroformylation of Olefins by a Rhodium Single-Atom Catalyst with Activity Comparable to $RhCl(PPh_3)_3$. *Angew. Chem., Int. Ed.* **2016**, *55*, 16054−16058.
(44) Alvarado Rupflin, L.; Mormul, J.; Lejkowski, M.; Titlbach, S.; Papp, R.; Gläser, R.; Dimitrakopoulou, M.; Huang, X.; Trunschke, A.; Willinger, M. G.; Schlögl, R.; Rosowski, F.; Schunk, S. A. Platinum Group Metal Phosphides as Heterogeneous Catalysts for the Gas-Phase Hydroformylation of Small Olefins. *ACS Catal.* **2017**, *7*, 3584−3590.
(45) Li, C.; Sun, K.; Wang, W.; Yan, L.; Sun, X.; Wang, Y.; Xiong, K.; Zhan, Z.; Jiang, Z.; Ding, Y. Xantphos Doped Rh/POPs-PPh_3 Catalyst for Highly Selective Long-Chain Olefins Hydroformylation: Chemical and DFT Insights into Rh Location and the Roles of Xantphos and PPh_3. *J. Catal.* **2017**, *353*, 123−132.
(46) Wang, L.-L.; Khare, S. V.; Chirita, V.; Johnson, D. D.; Rockett, A. A.; Frenkel, A. I.; Mack, N. H.; Nuzzo, R. G. Origin of Bulklike Structure and Bond Length Disorder of Pt_{37} and Pt_6Ru_{31} Clusters on Carbon: Comparison of Theory and Experiment. *J. Am. Chem. Soc.* **2006**, *128*, 131−142.
(47) Frenkel, A. I.; Yang, J. C.; Johnson, D. D.; Nuzzo, R. G. *Nanoscale Atomic Clusters, Complexity of BT—Encyclopedia of Complexity and Systems Science*; Meyers, R. A., Ed.; Springer New York: New York, NY, 2009; pp 5889−5912.
(48) Bianchi, C. L.; Ragaini, V.; Cattania, M. G. An XPS Study on Ruthenium Compounds and Catalysts. *Mater. Chem. Phys.* **1991**, *29*, 297−306.
(49) Kaga, Y.; Abe, Y.; Yanagisawa, H.; Kawamura, M.; Sasaki, K. Ru and RuO_2 Thin Films by XPS. *Surf. Sci. Spectra* **1999**, *6*, 68−74.
(50) Morgan, D. J. Resolving Ruthenium: XPS Studies of Common Ruthenium Materials. *Surf. Interface Anal.* **2015**, *47*, 1072−1079.
(51) Wagner, C.; Powell, C.; Allison, J.; Rumble, J. *NIST X-Ray Photoelectron Spectroscopy Database 1, Version 2. Nat'l Std. Ref. Data Series (NIST NSRDS)*; National Institute of Standards and Technology: Gaithersburg, MD, 1997.
(52) Lu, B.; Guo, L.; Wu, F.; Peng, Y.; Lu, J. E.; Smart, T. J.; Wang, N.; Finfrock, Y. Z.; Morris, D.; Zhang, P.; Li, N.; Gao, P.; Ping, Y.; Chen, S. Ruthenium Atomically Dispersed in Carbon Outperforms Platinum toward Hydrogen Evolution in Alkaline Media. *Nat. Commun.* **2019**, *10*, 631.
(53) Jarzembska, K.; Seal, S.; Woźniak, K.; Szadkowska, A.; Bieniek, M.; Grela, K. X-Ray Photoelectron Spectroscopy and Reactivity Studies of a Series of Ruthenium Catalysts. *ChemCatChem* **2009**, *1*, 144−151.
(54) Ohyoshi, A.; Götzfried, F.; Beck, W. Polynuclear carbonyl complexes of ruthenium and osmium with methylthiolate and bromide bridging ligands. *Chem. Lett.* **1980**, *9*, 1537−1540.
(55) Zhang, C.; Sha, J.; Fei, H.; Liu, M.; Yazdi, S.; Zhang, J.; Zhong, Q.; Zou, X.; Zhao, N.; Yu, H.; Jiang, Z.; Ringe, E.; Yakobson, B. I.; Dong, J.; Chen, D.; Tour, J. M. Single-Atomic Ruthenium Catalytic Sites on Nitrogen-Doped Graphene for Oxygen Reduction Reaction in Acidic Medium. *ACS Nano* **2017**, *11*, 6930−6941.
(56) Zhang, C.; Fu, L.; Liu, N.; Liu, M.; Wang, Y.; Liu, Z. Synthesis of Nitrogen-Doped Graphene Using Embedded Carbon and Nitrogen Sources. *Adv. Mater.* **2011**, *23*, 1020−1024.

https://doi.org/10.1021/acscatal.1c05737
ACS Catal. 2022, 12, 4182−4193

(57) Wang, H.; Maiyalagan, T.; Wang, X. Review on Recent Progress in Nitrogen-Doped Graphene: Synthesis, Characterization, and Its Potential Applications. *ACS Catal.* **2012**, *2*, 781−794.
(58) Ito, Y.; Christodoulou, C.; Nardi, M. V.; Koch, N.; Sachdev, H.; Müllen, K. Chemical Vapor Deposition of N-Doped Graphene and Carbon Films: The Role of Precursors and Gas Phase. *ACS Nano* **2014**, *8*, 3337−3346.
(59) Adeniyi, A. A.; Ajibade, P. A. Exploring the Ruthenium-Ligands Bond and Their Relative Properties at Different Computational Methods. *J. Chem.* **2016**, *2016*, 3672062.
(60) Planas, N.; Vigara, L.; Cady, C.; Miró, P.; Huang, P.; Hammarström, L.; Styring, S.; Leidel, N.; Dau, H.; Haumann, M.; Gagliardi, L.; Cramer, C. J.; Llobet, A. Electronic Structure of Oxidized Complexes Derived from Cis-$[Ru^{II}(Bpy)_2(H_2O)_2]^{2+}$ and Its Photoisomerization Mechanism. *Inorg. Chem.* **2011**, *50*, 11134−11142.
(61) Sardar, K.; Petrucco, E.; Hiley, C. I.; Sharman, J. D. B.; Wells, P. P.; Russell, A. E.; Kashtiban, R. J.; Sloan, J.; Walton, R. I. Water-Splitting Electrocatalysis in Acid Conditions Using Ruthenate-Iridate Pyrochlores. *Angew. Chem., Int. Ed.* **2014**, *53*, 10960−10964.
(62) Ratso, S.; Sougrati, M. T.; Käärik, M.; Merisalu, M.; Rähn, M.; Kisand, V.; Kikas, A.; Paiste, P.; Leis, J.; Sammelselg, V.; Jaouen, F.; Tammeveski, K. Effect of Ball-Milling on the Oxygen Reduction Reaction Activity of Iron and Nitrogen Co-Doped Carbide-Derived Carbon Catalysts in Acid Media. *ACS Appl. Energy Mater.* **2019**, *2*, 7952−7962.
(63) Le Goanvic, L.; Couturier, J.-L.; Dubois, J.-L.; Carpentier, J.-F. Ruthenium-Catalyzed Hydroformylation of the Functional Unsaturated Fatty Nitrile 10-Undecenitrile. *J. Mol. Catal. A: Chem.* **2016**, *417*, 116−121.
(64) Fleischer, I.; Wu, L.; Profir, I.; Jackstell, R.; Franke, R.; Beller, M. Towards the Development of a Selective Ruthenium-Catalyzed Hydroformylation of Olefins. *Chem.—Eur. J.* **2013**, *19*, 10589−10594.
(65) Corma, A.; Concepcion, P.; Dominguez, I.; Forne, V.; Sabater, M. Gold Supported on a Biopolymer (Chitosan) Catalyzes the Regioselective Hydroamination of Alkynes. *J. Catal.* **2007**, *251*, 39−47.
(66) Sabater, M. J.; Ródenas, T.; Heredia, A. Biopolymers from Plants. In *Handbook of Biopolymer-Based Materials: From Blends and Composites to Gels and Complex Networks*; Thomas, S., Durand, D., Chassenieux, C., Eds.; Wiley Online Books, John Wiley & Sons, Inc, 2013; pp 37−86.
(67) Simonelli, L.; Marini, C.; Olszewski, W.; Ávila Pérez, M.; Ramanan, N.; Guilera, G.; Cuartero, V.; Klementiev, K. CLÆSS: The Hard X-Ray Absorption Beamline of the ALBA CELLS Synchrotron. *Cogent Phys.* **2016**, *3*, 1231987.
(68) Ravel, B.; Newville, M. ATHENA, ARTEMIS, HEPHAESTUS: Data Analysis for X-Ray Absorption Spectroscopy Using IFEFFIT. *J. Synchrotron Radiat.* **2005**, *12*, 537−541.
(69) Rehr, J. J.; Albers, R. C. Theoretical Approaches to X-Ray Absorption Fine Structure. *Rev. Mod. Phys.* **2000**, *72*, 621−654.
(70) Bevington, P. R.; Robinson, D. K.; Blair, J. M.; Mallinckrodt, A. J.; Mckay, S. Data Reduction and Error Analysis for the Physical Sciences. *Cit. Comput. Phys.* **1993**, *7*, 415.
(71) Newville, M. EXAFS analysis usingFEFF and FEFFIT. *J. Synchrotron Radiat.* **2001**, *8*, 96−100.
(72) Newville, M. Larch: An Analysis Package for XAFS and Related Spectroscopies. *J. Phys. Conf. Ser.* **2013**, *430*, 12007.

https://doi.org/10.1021/acscatal.1c05737
ACS Catal. 2022, 12, 4182−4193